The Astrophysical Journal Letters, 890:L23 (12pp), 2020 February 20 https://doi.org/10.3847/2041-8213/ab72a4

Space Weathering Simulation with Low-energy Laser Irradiation of Murchison CM Chondrite for Reproducing Micrometeoroid Bombardments on C-type Asteroids

Moe Matsuoka[1], Tomoki Nakamura[2], Takahiro Hiroi[3], Satoshi Okumura[2], and Sho Sasaki[4]
[1] Japan Aerospace Exploration Agency (JAXA), Sagamihara, Kanagawa 252-5210, Japan; matsuoka.moe@jaxa.jp
[2] Tohoku University, Sendai, Miyagi 980-8578, Japan
[3] Brown University, Providence, RI 02912, USA
[4] Osaka University, Toyonaka, Osaka 560-0043, Japan
Received 2019 November 13; revised 2020 January 23; accepted 2020 February 1; published 2020 February 20

Abstract

Micrometeoroid bombardments are one of the causes of space weathering on airless bodies. We have simulated micrometeoroid bombardments on the surfaces of C-type asteroids by pulse-laser irradiation experiments on Murchison CM2 chondrite samples. In this Letter, we focus in particular on the effect of lower-energy irradiation compared to our previous study, where the laser energy range was set to 5–15 mJ, causing spectral flattening and water absorption band suppression. Murchison powder samples were irradiated with pulse lasers of various laser intensities (0.7, 1, 2, and 5 mJ). The irradiation energies are equivalent to micrometeoroid bombardments on the main-belt asteroids for $\sim 5.7 \times 10^7$ yr for 5 mJ and $\sim 7.9 \times 10^6$ yr for 0.7 mJ, respectively. We measured reflectance spectra and analyzed chemical compositions and microstructures of the surface of the laser-irradiated Murchison samples. Laser-irradiated Murchison spectra show flattening and darkening in the ultraviolet (UV)–visible (Vis)–infrared (IR) range. As the laser energy was increased up to 5 mJ, the 3 and 0.7 μm band depths decreased by 12% and 50%, respectively. The particle surface in the 5 mJ irradiated area shows melted and vesiculated structures, indicating high-temperature heating by laser irradiation followed by rapid cooling. The chemical composition of the melted and bubbled portions is similar to FeS-rich amorphous silicate particles observed in the high-energy laser irradiation case. Each mineralogical change of Murchison due to short-duration heating would cause spectral bluing, darkening, and absorption band suppression.

Unified Astronomy Thesaurus concepts: Carbonaceous chondrites (200); Spectroscopy (1558); Laboratory astrophysics (2004)

1. Introduction

Pulse-laser irradiation experiments using Murchison CM2 chondrite samples were previously performed to simulate micrometeoroid bombardments on C-type asteroids (Matsuoka et al. 2015). The laser energy levels used were 5, 10, and 15 mJ. After irradiation, hydrous minerals, such as serpentines and tochilinite, became amorphous and dehydrated due to short-duration heating. FeS-rich amorphous silicate splash particles generated were observed by a transmission electron microscope (TEM) analysis. Murchison spectra showed flattening and darkening as laser energy increases, and shallowing of the 0.7 μm band due to charge transfer between Fe^{2+} and Fe^{3+}, and the 3 μm band due to the O–H stretching mode (Ryskin 1974). Each spectral feature changed successively up to 15 mJ, while the darkening appeared to be saturated at 5 mJ. In this study, in order to observe more detailed stepwise spectral changes, focusing on the mineralogical and spectral changes of Murchison due to low-energy laser irradiation, we have performed laser irradiation experiments with laser energy lower than 5 mJ. To clarify the changes of mineralogy and spectra due to space weathering is important to detect the surface property and link remote sensed data with future returned samples obtained by JAXA's *Hayabusa2* and NASA's *OSIRIS-REx* spacecrafts.

2. Experiment

2.1. Sample Preparation and Pulse-laser Irradiation

A Murchison CM chondrite chip ($\sim 1\ cm^3$ in volume) was ground into fine powder (<63 μm in particle size). Two pellets were prepared with the Murchison powder pressed into copper dishes, and then irradiated with a Nd-YAG laser (1064 nm in wavelength) in vacuum of 10^{-5} torr. The pulse duration was 6–8 ns. The irradiated laser energies were 0.7, 1, 2, and 5 mJ for four different areas on two pellets: 0.7 and 5 mJ on pellet A, and 1 and 2 mJ on pellet B. The total energy delivery was 6, 8, 16, and 40 mJ mm^{-2} for 0.7, 1, 2, and 5 mJ, respectively. See Yamada et al. (1999) and Matsuoka et al. (2015) for more details on the experimental conditions. Spectral data of this work and previous work are available in the RELAB database.[5] See the Appendix.

2.2. Reflectance Spectra Measurements

Reflectance spectra were measured after irradiation experiments. Visible and near-infrared (VNIR) diffuse bidirectional reflectance spectra were measured over 0.25–2.5 μm in wavelength at every 5 nm at the Mizusawa Very Long Baseline Interferometry (VLBI) Observatory of National Astronomical Observatory of Japan (NAOJ). The incidence and emission angles were 30° and 0°, respectively. The measured surface area was 2 mm × 3 mm in size. The reference standard was Spectralon (SRS99 from Labsphere). The samples were heated to approximately 100°C in ambient air during measurements to remove the effect of adsorbed water.

Fourier-transform infrared (FT-IR) reflectance spectra of the samples were measured over 4000–700 cm^{-1} (~2.5–14 μm in wavelength) at every 1.9 cm^{-1} using Thermo Fisher Scientific

[5] http://www.planetary.brown.edu/relab

Nicolet iN10 with OMNIC Picta software at Tohoku University, Japan. The incidence and emission angles were 0° each. The measured surface area was 400 × 400 μm in size. The reference standard was a gold mirror. The samples were heated to approximately 100°C and purged in N_2 gas during measurements in order to remove the effects of atmospheric water and CO_2, and adsorbed water. The average spectra of four or five points each of the irradiated areas were taken as representative spectra. The FT-IR spectra were scaled and spliced to the VNIR spectra at 2.5 μm by multiplying by a scaling factor because the VNIR spectra have more reliable albedo values.

The detailed analytical conditions and measurement procedures are described in Matsuoka et al. (2015).

2.3. Field Emission Scanning Electron Microscope (FE-SEM) Observation

The surface structures and chemical compositions of pellet samples were analyzed using an FE-SEM equipped with an energy dispersive X-ray spectrometer (EDS), JEOL JSM-7001F at Tohoku University. The surface powders were picked up from the 5 mJ irradiated region at the surface of pellet A, fixed on the carbon tape, and used for FE-SEM and EDS analyses. The focused beam analysis was performed to identify the variation of chemical composition in micrometer scale.

2.4. Raman Spectra Measurements

Raman spectra were measured using JASCO NRS-5100 with a 532 nm exciting laser radiation at Tohoku University. The laser was focused on the pellet surface using an objective lens (×20). Two scans with 60 s each were performed for the measurements. The spectral resolution was 1 cm^{-1}, and the spot size was 5 μm. The peak fitting was operated using the Gaussian function after subtraction of the linear continuum using Lightstone Corp. Origin software.

3. Results

3.1. Ultraviolet (UV)–Visible (Vis)–Infrared (IR) Reflectance Spectra

Reflectance spectra of Murchison pellet samples show decreases in albedo, slope, and absorption band strength with increasing laser energy (Figures 1(a)–(c)). Reflectance at the shortest wavelength of 0.25 μm decreases (e.g., 0.7 and 1 mJ) and then increases (e.g., 2 and 5 mJ) as shown in Figure 1(c). The 0.55 μm reflectance decreases with increasing laser energies up to 5 mJ (Table 1). The spectral slope in the shorter wavelength range decreases continuously with laser energy increasing from 0 to 5 mJ (Table 1).

The 3 and 0.7 μm bands are well identified in all spectra and both bands become shallower as laser energy increases (Figures 1(a)–(c)). The 3 μm band center and depth are defined at the deepest point after continuum removal, and the 0.7, 0.9, and 1.1 μm band center, width (FWHM), and strength are derived from modified Gaussian fitting (Figures 1(d) and (e)). See the Appendix and Hiroi et al. (2000) for more details of the fitting procedure. The results are summarized in Table 1. The 3 μm band depth decreases by ∼14% at 5 mJ (Figures 1(a)–(d) and Table 1), which is mostly consistent with the results of the previous study (e.g., ∼17% less at 5 mJ in Matsuoka et al. 2015). The 3 and 0.7 μm band center and the FWHM values of the 0.7 μm band show no significant changes (Table 1).

Figures 1(b) and (f) show two types of the 10 μm bands, namely, the Reststrahlen bands (RBs): the first type shows two peaks at ∼11.3 and ∼12.3 μm appear in the 0, 0.7, and 1 mJ spectra consistent with the reflectance spectra of Murchison obtained by Salisbury et al. (1991) and McAdam et al. (2015), which reported NIR–MIR spectra of powdered Murchison, while the second type has one prominent peak around 10.5 μm in the 2 and 5 mJ spectra similar to the Murchison reflectance spectra measured by Lantz et al. (2015, 2017).

3.2. FE-SEM Observation

Several Murchison grains of ∼60 μm in diameter were collected with a needle selected from the 5 mJ irradiated area under a microscope and analyzed using FE-SEM/EDS (Figures 2(a)–(d)). The entire surface of the grain is covered with micrometer-size melted and vesiculated particles forming a rough surface (Figures 2(a)–(d)). Figures 2(b)–(d) show the magnified image of the melted/bubbled structures ∼1 μm diameter, produced due to heating above the melting points of silicates in the matrix followed by rapid cooling. Ameba-like "sticky structures" having a smooth surface are observed relatively beneath the sample surface (e.g., Figure 2(c)), while globular structures <1 μm in diameter are distributed at the surface of the grain (e.g., Figure 2(b)).

The S/Fe/(Mg+Si) ratios of the melted/bubbled structures are shown in Figures 2(e)–(f). Both sticky and globular structures are Fe- and S-rich, which is consistent with those of FeS-rich amorphous silicate splash particles captured from 15 mJ irradiated Murchison analyzed in Matsuoka et al. (2015).

3.3. Raman Analysis

Raman spectroscopy is a sensitive technique to detect the maturation grade of organic matter (OM). The *G* band is due to the E_{2g2} vibrational mode of the aromatic plane, and the *D* band is due to structural disorder. Figure 3 shows that Raman spectra of unirradiated and irradiated areas of Murchison pellets have *D* and *G* bands at ∼1355 and ∼1589 cm^{-1}. The intensity ratio of the *D* and *G* bands does not show any significant change as laser energy increases even to the highest energy, 5 mJ (Table 1). The Raman spectral parameters are consistent with virgin Murchison measurement results by Busemann et al. (2007). It would indicate that carbonization did not promote significantly by short-duration heating in this study, because carbonization effectively proceeds by long-duration heating (e.g., Busemann et al. 2007; Basu 2010; Zhao et al. 2010; Mahapatra et al. 2015).

4. Discussion

Figures 4(a)–(f) show several spectral parameter values of Murchison spectra as a function of irradiated laser energy. Reflectance spectra of Murchison irradiated with 0.7–15 mJ show darkening (Figure 4(a)) and flattening (Figure 4(b)), and the 0.7 and 3 μm band depth decreases (Figures 4(c)–(d)). As seen in Figure 4(a), darkening at 0.55, 0.90, and 2.50 μm is almost stopped at ∼5 mJ, while other features change proportional to laser energy.

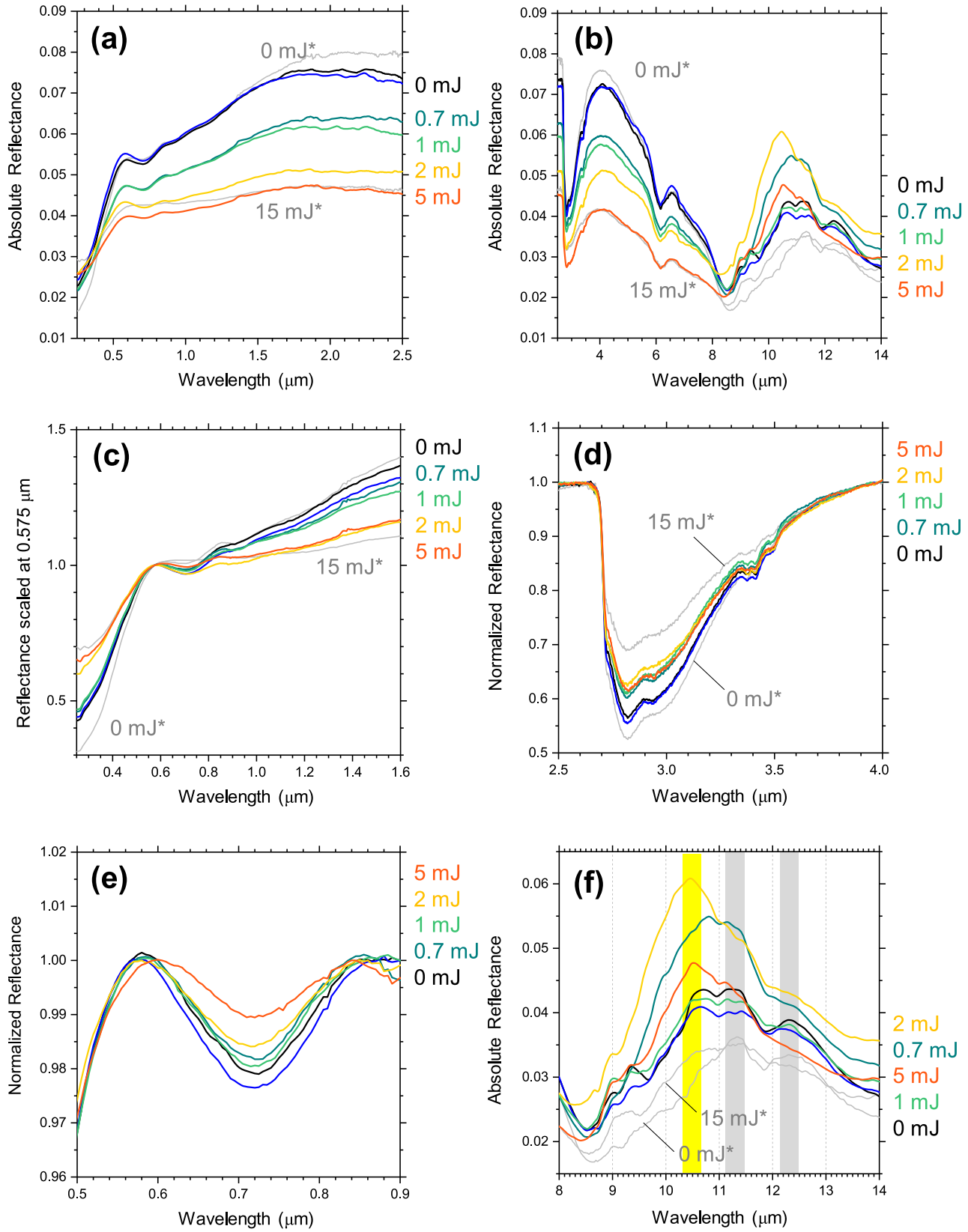

Figure 1. Vis–MIR spectra of Murchison samples over the ranges of 0.25–2.5 μm (a), 2.5–14 μm (b), and 0.25–1 μm (c). The reflectance and UV slope decreases with laser energy increasing. Normalized spectra of the 3 μm band (d) and the 0.7 μm band (e). Both absorption band depths become shallower with laser energy increasing. Continuum removal is performed by the same procedure described in detail by Matsuoka et al. (2015). The MIR spectra of Murchison samples over the range of 8–14 μm (f). 0 mJ shows the spectra of unirradiated samples. Gray spectra (15 and 0 mJ) in Matsuoka et al. (2015) are plotted together for comparison.

Table 1
Reflectance and Raman Spectral Parameters of Murchison Samples Irradiated at 0.7–5 mJ

	Laser Energy					
	0 mJ A[a]	0 mJ B[b]	0.7 mJ	1 mJ	2 mJ	5 mJ
3 μm band center (μm)	2.820 ± 0.002[c]	2.818 ± 0.003	2.820 ± 0.005	2.813 ± 0.004	2.818 ± 0.006	2.824 ± 0.006
3 μm band depth (%)	43.6	44.6	39.9	39.1	37.6	38.6
0.7 μm band center (μm)	0.726	0.730	0.721	0.723	0.726	0.724
0.7 μm band depth	0.069	0.081	0.058	0.062	0.058	0.032
FWHM (μm)	0.183	0.199	0.165	0.174	0.187	0.139
0.9 μm band center (μm)	0.948	0.939	0.933	0.933	0.945	0.977
0.9 μm band depth	0.035	0.035	0.033	0.027	0.040	0.030
FWHM (μm)	0.154	0.140	0.133	0.140	0.183	0.234
1.1 μm band center (μm)	1.157	1.139	1.144	1.144	1.184	1.219
1.1 μm band depth	0.037	0.038	0.039	0.033	0.033	0.024
FWHM (μm)	0.252	0.280	0.321	0.292	0.306	0.232
Reflectance at 0.55 μm	0.053	0.054	0.046	0.047	0.043	0.039
Reflectance at 0.35 μm	0.030	0.031	0.028	0.028	0.030	0.028
Reflectance at 0.90 μm	0.058	0.058	0.050	0.050	0.044	0.041
Spectral slope (μm^{-1}) over the 0.35–0.90 μm range	0.050	0.048	0.040	0.040	0.024	0.023
Peak_D (cm^{-1})	1356.1	1355.3	1355.2	1354.7	1354.4	1356.6
Width_D (cm^{-1})	268.8	277.1	270.3	269.8	272.6	273.9
Peak_G (cm^{-1})	1584.6	1585.7	1588.1	1586.4	1587.0	1586.9
Width_G (cm^{-1})	101.6	93.2	92.0	97.3	96.4	95.5
I_D/I_G	0.947	0.936	0.919	0.940	0.945	0.931

Notes.
[a] Virgin area of pellet irradiated at 1 and 2 mJ.
[b] Virgin area of pellet irradiated at 0.7 and 5 mJ.
[c] 1σ variation of four or five analysis data.

4.1. Mineralogical Change due to Laser Heating

At the sample surface, as described by Bennett et al. (2013), within a short time focused energy is derived on the irradiation point, then hydrous silicates are rapidly heated up. Serpentines and tochilinite are vaporized, and at the deeper area, dehydration proceeds quickly and incompletely. Several components produced by laser heating would be deposited on the surface of Murchison powder grains, and contribute to spectral changes based on the FE-SEM analysis of laser-irradiated pellet surface performed in this study and TEM analysis of the melted material (Matsuoka et al. 2015). Estimating from the size of vesicles and splash particles (e.g., Figures 2(b)–(d); a few ~100 nm in diameter typically), the dehydrated layer can grow to the submicrometer thickness due to laser heating. Each component stacking over the original grain surface is as follows from the upper region;

(I) Splash particles generated from the vapor phase. Fine amorphous silicate particles <50 nm are possibly the carbon-free vapor deposit based on their similar chemical compositions with relatively high Fe and S ratios and large particle sizes (Matsuoka et al. 2015).
(II) Splash particles formed from the melt. Amorphous silicate particles >50 nm found by Matsuoka et al. (2015) are deposited at the grain surface of the 5 mJ irradiated Murchison sample (e.g., globular structures in Figure 2(d)). These particles are enriched in Fe and S compared with those of the average of Murchison unirradiated areas. These particles would be formed from the melted layer described below as Component (III) and distributed over the sample surface.
(III) Melted layer enriched in Fe and S (Figures 2(a)–(d)). In this layer, preferential melting of hydrous minerals occurs in the S- and Fe-rich region, especially tochilinite-rich areas, due to their relatively low melting point as described in Matsuoka et al. (2015). In this layer silicates are dehydrated and thus show no water absorption at around 3 μm in the spectrum. At the outermost surface of this layer, melted and bubbled structures were developed (e.g., globular structures in Figures 2(b)–(d)), which have similar chemical composition (FeS-rich) and particle size (up to sub-μm size) to the splash particles (Figures 2(b)–(f)). The formation of globular structures, possibly remnants of splash particles that could not escape and remain stuck, may increase microroughness on grain surfaces.
(IV) Amorphous layer. In this layer, amorphization and decomposition of serpentines and tochilinite occur at sub-solidus temperature. These hydrous phases become dehydrated incompletely during laser irradiation by indirect heating due to heat transfer from the neighboring upper melted material.

In proportion to laser energy with which Murchison samples are irradiated, the thickness of layers (III) and (IV) and the population of particles (I) and (II) should increase, thus the spectral change could increase successively up to 15 mJ irradiation.

4.2. Spectral and Mineralogical Change Caused by Laser Heating

4.2.1. Albedo Change

Figure 4(a) shows that darkening proceeds drastically over the range of <5 mJ but saturates at >5 mJ. It is possibly explained by the layer thickness ratio development that Components (I)–(III)

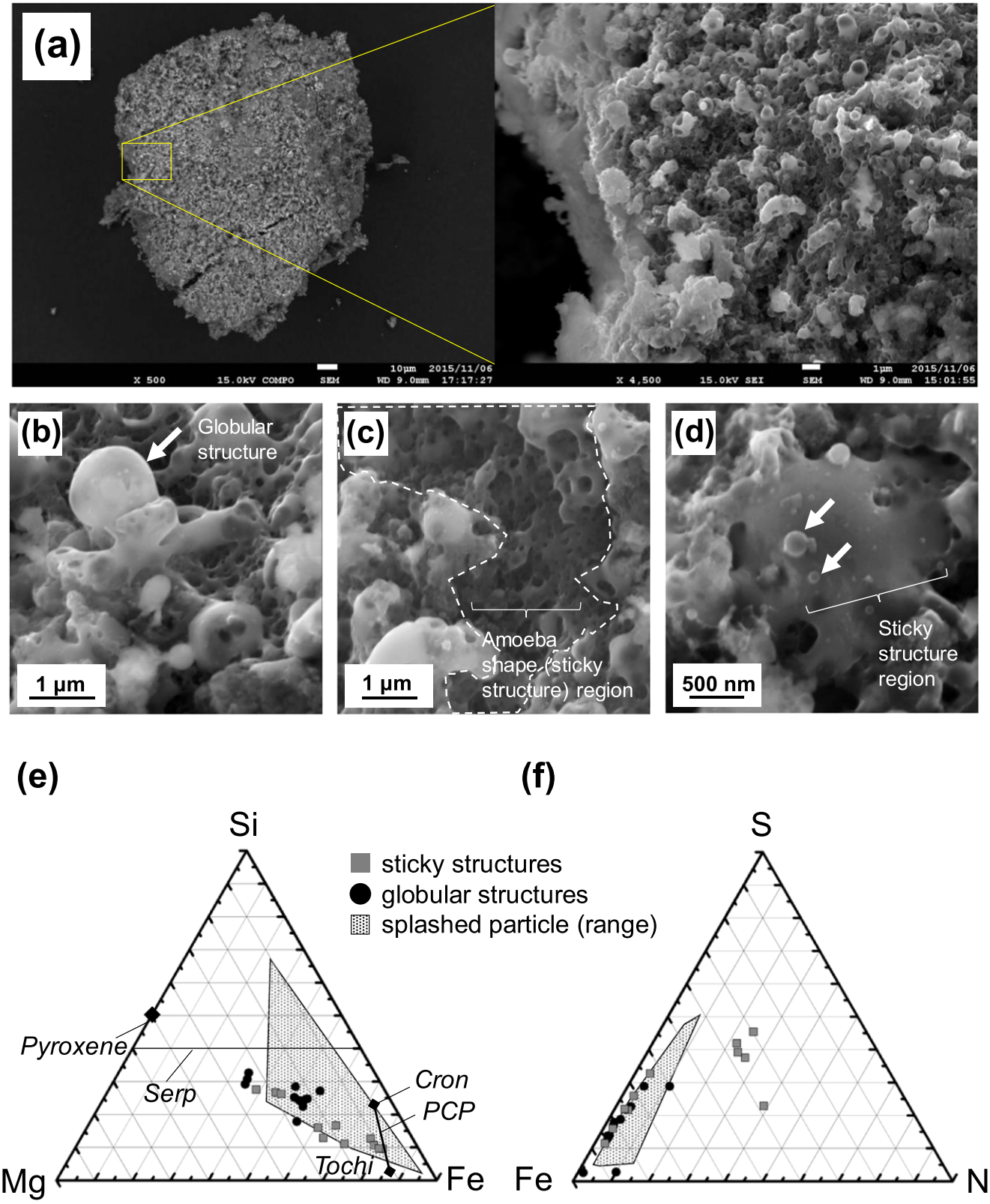

Figure 2. SEM composition image of the 5 mJ irradiated Murchison powder particle (a). Right figure shows magnified secondary electron image of the square range of the left panel. Secondary electron image showing melting and bubbling structures with globular (indicated by an arrow) (b) and ameba shapes (surrounded by dotted line) (c) of silicates by laser irradiation at the surface of the powder particle. Several sub-micrometer-size splash particles indicated by arrows are deposited on the sticky structure (d). Ternary graphs of Si–Mg–Fe system (e) and S–Fe–Ni system (f) with atomic ratios of the particles of the 5 mJ sample. The FeS-rich compositions are similar among sticky structures (ameba-shape structures; gray square)/globular structures (black circle) at the surface of the 5 mJ particle in this study and also splashed particles (range) analyzed in Matsuoka et al. (2015). Abbreviations: serpentine (Serp), cronstedtite (Cron), and tochilinite (Tochi).

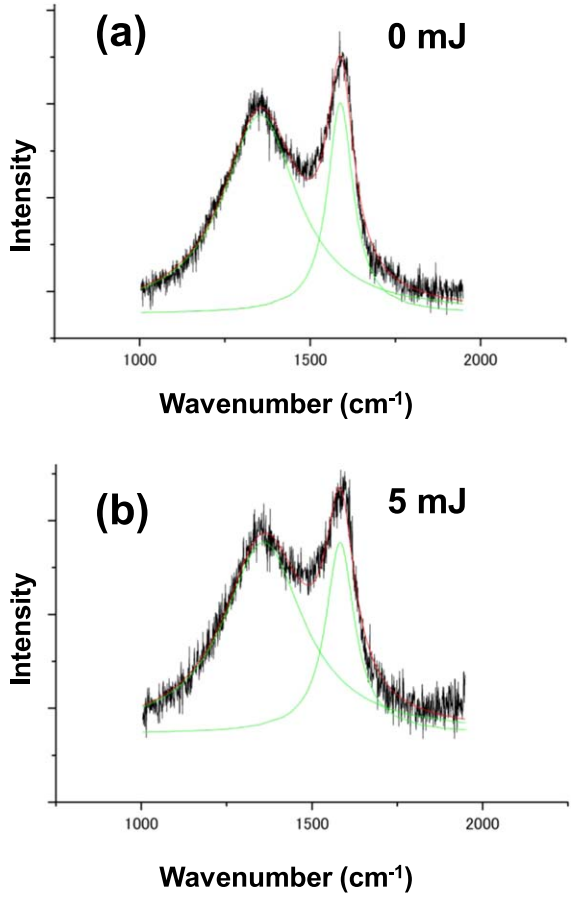

Figure 3. Two typical Raman spectra of 0 mJ (a) and 5 mJ (b) samples. *D* and *G* bands are present at ∼1350 and ∼1600 cm^{-1}.

increase and thus the upper edge of Component (IV) becomes deeper. Then, the contribution of melted layers of Components (I)–(III) to the reflectance spectral property becomes dominant.

Darkening of laser-irradiated Murchison spectrum was caused by the development of Components (III) and (IV). Terrestrial serpentines and tochilinite originally have high reflectance (>30% at 0.55 μm; Hiroi & Zolensky 1999; RELAB data shown in Cloutis et al. 2011), and amorphization and decomposition of these minerals reduce the albedo (Hiroi & Zolensky 1999). In addition, the splash particles of Component (II) also contribute spectral darkening. Component (II) particles mainly have a diameter of >∼100 nm (Figures 2(b), (c)), and Noble et al. (2007) suggest that Fe^0 particles >40 nm in diameter (up to ∼200 nm in their study) make spectra darker. In our experiments, sulfide-like Components (I) and (II) can contribute to spectral darkening. We observed Fe–S-rich sticky/globular structures and splash particles on the surfaces of 5 and 15 mJ irradiated samples (Figures 2(b)–(f) in this study; Matsuoka et al. 2015). Sulfide minerals, such as pyrrhotite $Fe_{1-x}S$ (∼3% at 0.55 μm), pentlandite $(Fe, Ni)_9S_8$ (∼7% at ∼0.55 μm), and troilite FeS (∼5% at ∼0.55 μm), have relatively low reflectance (Cloutis et al. 2011). Thompson et al. (2019a) reported that in Murchison slab samples deposit materials that were produced by laser irradiation and captured on the glass slide show featureless and a red-sloped spectrum that is similar to spectra of pentlandite and troilite, still the relative reflectance measured overlaid on Spectralon is high (∼70% at 0.60 μm). Nanophase and microphase magnetite particles can cause spectral darkening and bluing (Thompson et al. 2019b), but magnetite was not identified in this study. In addition, the ameba-like region of Component (III) is smooth as shown in Figure 2(c) and effective for specular reflection, and contributes to decreasing diffuse reflectance.

Brightening possibly occurred simultaneously due to the μm-order roughness due to the production of sticky/globular structures on the sample surface and the increase in bubble density within the inner layer, which is effective for the enhancement of diffuse reflectivity (Figures 2(a)–(d)). Cancellation between darkening and brightening processes possibly caused the darkening saturation of Murchison spectra irradiated 5–15 mJ.

4.2.2. Spectral Slope Decrease

A red spectral slope of virgin Murchison spectra over the 0.35–0.90 μm wavelength range shown in Figures 1(a) and (c), and Table 1 is a shoulder of an UV absorption and possibly due to Fe–O and Ti–O charge transfers (Cloutis et al. 2008), and/or polycyclic aromatic hydrocarbons (PAHs) due to π–π^* plasmon resonance in PAH components (Duley & Lazarev 2004; Moroz et al. 2004).

The 0.35–0.90 μm slope of Murchison decreases continuously as laser energy increases (Figure 4(b)). Components (III) and (IV) could contribute to the slope decrease. Amorphization and decomposition of Fe-rich hydrous silicates weaken a positive slope that hydrous silicates originally had. In contrast, Components (I) and (II) can contribute to spectral reddening as Thompson et al. (2019a) reported that Fe–Ni–sulfide particles <∼50 nm in size deposited by laser heating showed the red-slope spectrum. Because major minerals in the Murchison matrix are hydrous silicates (84.6 vol% as sum of pentlandite, serpentine, and cronstedite/tochilinite; based on Bland et al. 2004), dehydration and amorphization at the matrix can more effectively contribute to the spectral change (bluing) because of its larger and deeper occupied space than production of Components (I) and (II) (reddening). Therefore, the Murchison spectrum becomes flatter over the 0.35–0.90 μm wavelength range as irradiated laser energy increases.

The spectral slope over the 0.35–0.55 μm wavelength range decreased due to laser irradiation by up to ∼53% (5 mJ; Figures 1(c) and 4(b)). Carbon structure changes such as graphitization effect on spectra has been reported (e.g., Moroz et al. 2004; Brunetto et al. 2009; Lantz et al. 2017; Thompson et al. 2019a). In this study, UV reflectance increased (2.4% and 2.6% for 0 and 5 mJ at 0.25 μm) by ∼10%, and slope becomes flatter, which is a similar spectral response to the carbonization process explained by Moroz et al. (2004) and Lantz et al. (2017). The *D* bandwidth Γ_D, the *G* bandwidth Γ_G, and the intensity ratio of the *D* and *G* bands, I_D/I_G, can be useful for determining the degree of thermal metamorphism (Busemann et al. 2007); with increasing thermal metamorphism, Γ_D decreases and I_D/I_G increases simultaneously. In this study, however, Raman spectral parameters did not show any significant difference between virgin and laser-irradiated samples (Figure 4(f) and Table 1), indicating no obvious thermal alteration trend. Therefore, the spectral flattening of irradiated Murchison might not be explained well by the graphitization process due to laser heating. We performed Raman analyses on 4–5 points in each irradiated area selected randomly, then some points could measure a possible virgin region, which possibly occupies up to ∼30% in the irradiated area.

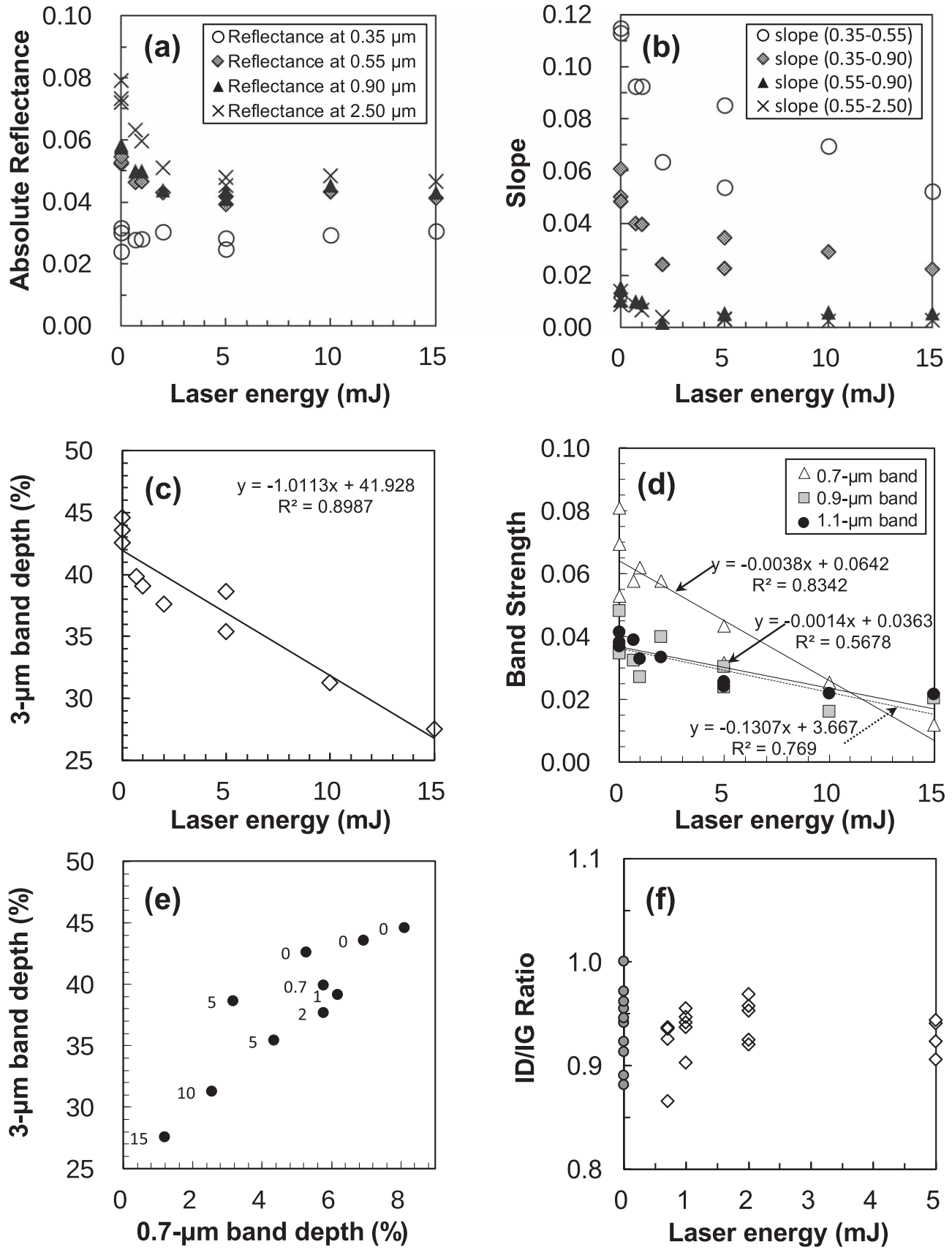

Figure 4. Relationship between the laser energy and the reflectance values at 0.35, 0.55, 0.90, and 2.50 μm (a), slopes (b), the band depths of the 3 μm band (c), and the band depths of the 0.7, 0.9, and 1.1 μm bands (d), and the depths of the 0.7 μm and the 3 μm bands (e) of reflectance spectra, and intensity ratio of *D* and *G* bands of Raman spectra (f). Numbers stand for the irradiated laser energy value (mJ).

4.2.3. Absorption Band Suppression

Fe-rich phyllosilicates and tochilinite spectra have significant 3 and 0.7 μm absorption bands (Cloutis et al. 2011 and references therein; Hiroi & Zolensky 1999; Sato 2017). Unirradiated Murchison spectra show the strong absorption bands at 3 and 0.7 μm (Figures 1(a)–(e), 4(c)–(e)). Then 3 and 0.7 μm band depth decreases continuously from 0 to 5 mJ (Figures 4(c)–(e)), and also up to 15 mJ irradiation (Matsuoka et al. 2015). Dehydration of hydrous silicates caused by laser heating decreased the 3 μm OH band depth. Decomposition of Fe-rich serpentine and tochilinite weakened the 0.7 μm band due to the Fe^{2+}–Fe^{3+} charge transfer feature. Components (III) and (IV) mainly contributed to these effects by dehydration and decomposition of hydrous silicates. Components (I) and (II), having no/weak absorption feature, also weaken the 3 and 0.7 μm absorption bands.

4.3. Comparison Between Laser-irradiation and Ion-irradiation Experiments

Interestingly, ion- and laser-irradiated carbonaceous chondrites show different spectral changes in the Vis–IR range, depending on the experimental conditions and also subtypes of chondrites. Murchison spectra showed reddening after 4 keV He^+ ion irradiation with up to 1×10^{18} ions cm^{-2} (Keller et al. 2015) and no change after 40 keV He^+ and Ar^+ ions irradiation with up to 3×10^{16} ions cm^{-2} (Lantz et al. 2015), and furthermore bluing (flattening) due to laser irradiation (this study; Matsuoka et al. 2015; Thompson et al. 2019b). On the other hand, Tagish Lake spectra showed bluing commonly after 40 keV He^+ ion irradiation with up to 6×10^{16} ions cm^{-2} (Lantz et al. 2017) after 4 keV Ar^+ ion irradiation with up to 10^{19} ions cm^{-2} (Vernazza et al. 2013), and also due to laser irradiation up to 5 mJ (Hiroi et al. 2013). Allende spectra showed reddening after 40 keV He^+ ion irradiation with up to 3×10^{16} ions cm^{-2} (Brunetto et al. 2014) and after 400 keV Ar^{++} ions irradiation with up to 9.4×10^{15} ions cm^{-2} (Lazzarin et al. 2006), and also due to repeated 30 mJ laser irradiation (Gillis-Davis et al. 2017). Meteorite Hills (MET) 01072 CM chip and pressed powder and Yamato (Y) 980115 CI pressed powder spectra showed bluing and only Y 980115 chip sample showed slight reddening after 20 keV He^+ ion irradiation with up to 6×10^{16} ions cm^{-2} (Nakamura et al. 2019).

Based on Lunar dust flux (1.9×10^{-16} g cm^{-2} s^{-1}; Bruno et al. 2007), the dust flux changes in proportion of $r^{-1.84}$, where r is the heliocentric distance (calculated based on Kelsall et al. 1998), then at ~2.5 au dust flux is calculated as ~0.2×, 3.5×10^{-17} g cm^{-2} s^{-1} = 1.1×10^{-9} g cm^{-2} yr^{-1}. When $\sim 10^{-11}$ g, equivalent to a few μm in size, is considered as the typical size of a micrometeoroid, the derived energy from dust impacts at the surface of airless body is calculated as 7.1×10^{-4} J m^{-2} yr^{-1}. Pulsed laser energy of 5 mJ irradiation deposits $\sim 4 \times 10^4$ J m^{-2} calculated based on Yamada et al. (1999). Then 5 mJ laser energy irradiation can simulate $\sim 5.7 \times 10^7$ yr of aging due to micrometeoroid bombardments at 2.5 au.

For ion irradiation using Murchison, (1) the amorphization of the phyllosilicates, (2) the growth of void structures (50–100 nm in size), (3) OH loss from hydrous silicates, and (4) the production of nanophase (2–5 nm in size) Fe-rich inclusions within the amorphous phyllosilicates occurred in the matrix (Keller et al. 2015). For laser irradiation experiments, (1), (2), and (3) proceed. In contrast, the size of (2), corresponding to Components (I) and (II), is larger compared to ion-irradiated samples. Also, ~15 nm diameter Fe grains, larger than (4), were observed in 15 mJ irradiated Murchison in ~5 to ~10 μm depth from the surface (Matsuoka 2015). Carbon loss and carbonization did not proceed significantly by the laser irradiation. We are aware that, in the space environment, mineralogical properties are not the only factor for spectral responses. In the case of ion-irradiation experiments, Nakamura et al. (2019) pointed out that even when using common carbonaceous chondrite samples spectral changes differently depend on the physical condition of the irradiated sample and energy level.

Therefore, due to ion/laser irradiations, spectral bluing of carbonaceous chondrites can be promoted by amorphization of hydrous silicates and production of FeS-rich amorphous silicate particles; spectral reddening of carbonaceous chondrites possibly are proceeded by amorphization of anhydrous silicates and production of nanophase iron particles.

4.4. Comparison among Asteroids Ryugu, Bennu, and Laser-irradiated Murchison

Asteroids Ryugu and Bennu, target asteroids of sample-return missions of JAXA's *Hayabusa2* and NASA's *OSIRIS-REx*, respectively, have been observed in the Vis–IR range using ground-based telescopes and spacecraft instruments. Both asteroids are very dark compared with the Murchison sample whose laboratory reflectance is around 5% (Table 1). Ryugu's reflectance factor, which is a calculated value in the same viewing geometry of 30° incident, 0° emission, and 30° phase angles as laboratory data, is 1.88% ± 0.17% at 0.55 μm (Sugita et al. 2019 geometric albedo is 4.5% ± 0.2%), and Bennu's reflectance factor is ~2.1% (Lauretta et al. 2019 geometric albedo is 4.4% ± 0.2%; Hamilton et al. 2019; Hergenrother et al. 2019). For hydrous mineral features, the 0.7 μm absorption band of Ryugu was detected by Vilas (2008), and may possibly be seen in disk-resolved spectra taken by the ONC-T instrument on board *Hayabusa2* (Sugita et al. 2019). On the other hand, Bennu shows no obvious band at 0.7 or 1.0 μm (Clark et al. 2011; Hamilton et al. 2019). The 3 μm absorption band is centered at around 2.72 μm for Ryugu, and 2.74 μm for Bennu. Although Ryugu's Vis–IR spectra do not exactly match any lab spectra of carbonaceous chondrites in the reflectance and blue UV–Vis slope, spectra of moderately heated CI (Hiroi et al. 1996) and shocked CM show some similarities (Kitazato et al. 2019). Our laser irradiation experiments produced spectral darkening and continuous bluing and band weakening for hydrous CM (Murchison). The spectral modification observed in this study could occur on the surface of CM-parent bodies, namely, dark and hydrous small bodies, and possibly contribute to the current spectra of Bennu. Because the surface materials on Ryugu are assumed to be much more dehydrated than Murchison used in our study, applying our results of laser irradiation experiments to the case of Ryugu may be difficult.

5. Conclusions

In conclusion, UV–Vis–IR spectra of Murchison samples irradiated with a pulse laser of 0.7–5 mJ in energy show bluing (flattening), darkening, and 0.7 and 3 μm absorption band suppression. These spectral changes are consistent with the change of Murchison spectra irradiated at 5–15 mJ in our previous study, except successive darkening in spectra of low-energy irradiated Murchison up to 5 mJ irradiation. Serpentine

dehydration and amorphization and the deposition of melted FeS-rich particles fabricated by laser heating would cause spectral bluing and darkening. Darkening caused by serpentine dehydration and amorphization would be canceled with brightening possibly due to surface roughness and inner vesicle density development by dynamic and rapid melting during high-temperature and short-duration heating.

We wish to thank Dr. M. Nakamura, Dr. M. Nemoto, Mr. T. Hirowatari, and Dr. K. Tsumura for technical supports during the FT-IR measurement, the Raman analysis, and sample preparation, and helpful advice for discussion, respectively. This research is supported by Japan Society for the Promotion of Science (JSPS) Core-to-Core Program "International Network of Planetary Sciences" and JSPS Grant-in-Aid for Scientific Research on Innovative Areas (Aqua Planetology, grant No. JP17H06459). We finally thank Dr. E. Cloutis for his helpful comments to improve this Letter.

Appendix

A.1. Data Information

Our spectral data in this study and Matsuoka et al. (2015) are registered in the RELAB database with the Sample IDs and Spectrum IDs listed in Table 2. These data are available for public use in the RELAB database.

A.2. Methods and Results of MGM Fitting Applied for 0.7, 0.9, and 1.1 μm Absorption Bands

Murchison spectra show 0.9 and 1.1 μm crystal field absorption bands due to Fe^{2+} in a single crystallographic site in addition to 0.7 μm absorption due to charge transfer between Fe^{2+} and Fe^{3+} in adjacent sites (Clark et al. 1990; Cloutis et al. 2011). To examine the change of the Fe-bearing-silicate-related absorption band properties, we performed Gaussian fitting using laser-irradiated Murchison spectra (0, 0.7, 1, 2, and 5 mJ of this study; 0, 5, 10, and 15 mJ of Matsuoka et al. 2015) after continuum removal. The continuum was linear with tangent points set at ~0.6 and ~1.5 μm. Then three bands centered at ~0.7, 0.9, and 1.1 μm were fit, and the depth, FWHM, and center wavelength of each Gaussian curve were calculated based on the procedure described in Hiroi et al. (2000). Fitting results are shown in Figures 5(a)–(j) and Table 1. The band centers located at 0.72–0.76, 0.93–0.98, and 1.14–1.24 μm, and within these ranges showed slight shifts toward longer wavelengths with increasing laser energy, and the strength of all three bands continuously decreases (Figures 4(d), 5(k), (l)). Compared to the 0 mJ Murchison average, the band strengths of 5 mJ irradiated Murchison in this study are 46.7%, 77.3%, and 62.5% for 0.7, 0.9, and 1.1 μm absorption bands, respectively. The FWHM values of 0.7 and 1.1 μm absorption bands are almost stable, though the FWHM of the 0.7 μm band slightly increases. These band changes possibly suggest that (1) the amount of Fe^{2+}- and Fe^{3+}-bearing silicates decreases continuously due to decomposition and amorphization, and/or (2) iron ions are reduced to form Fe grains observed by Matsuoka (2015). Both (1) and (2) proceeded due to laser irradiation that can be effective particularly for the Fe^{3+}-bearing phyllosilicate, cronstedtite. However, 10 mJ Murchison showed relatively large FWHM values of 0.9 and 1.1 μm band properties, which can be caused by low quality of fitting using a linear baseline and/or exposure of the other mineral grain such as olivine due to laser irradiation. We are aware that detailed analyses will be more useful using higher-resolution data in the future.

Table 2
Sample IDs and Spectrum IDs of Data Used in This Work and Matsuoka et al. (2015)

Sample Name	Sample ID	Spectrum ID		
		VNIR	FTIR	VNIR+FTIR
Murchison <63 μm pellet	MP-TXN-305	C1MP305	BMR1MP305	BKR1MP305
Murchison <63 μm pellet+Pulse laser 10 mJ	MP-TXN-305-L10	C1MP305L10	BMR1MP305L10	BKR1MP305L10
Murchison <63 μm pellet+Pulse laser 15 mJ	MP-TXN-305-L15	C1MP305L15	BMR1MP305L15	BKR1MP305L15
Murchison <63 μm pellet+Pulse laser 5 mJ	MP-TXN-305-L05	C1MP305L05	BMR1MP305L05	BKR1MP305L05
Murchison <63 μm pellet A	MP-TXN-306	C1MP306	BMR1MP306	BKR1MP306
Murchison <63 μm pellet A+Pulse laser 1 mJ	MP-TXN-306-L01	C1MP306L01	BMR1MP306L01	BKR1MP306L01
Murchison <63 μm pellet A+Pulse laser 2 mJ	MP-TXN-306-L02	C1MP306L02	BMR1MP306L02	BKR1MP306L02
Murchison <63 μm pellet B	MP-TXN-307	C1MP307	BMR1MP307	BKR1MP307
Murchison <63 μm pellet B+Pulse laser 0.7 mJ	MP-TXN-307-L01	C1MP307L01	BMR1MP307L01	BKR1MP307L01
Murchison <63 μm pellet B+Pulse laser 5 mJ	MP-TXN-307-L05	C1MP307L05	BMR1MP307L05	BKR1MP307L05

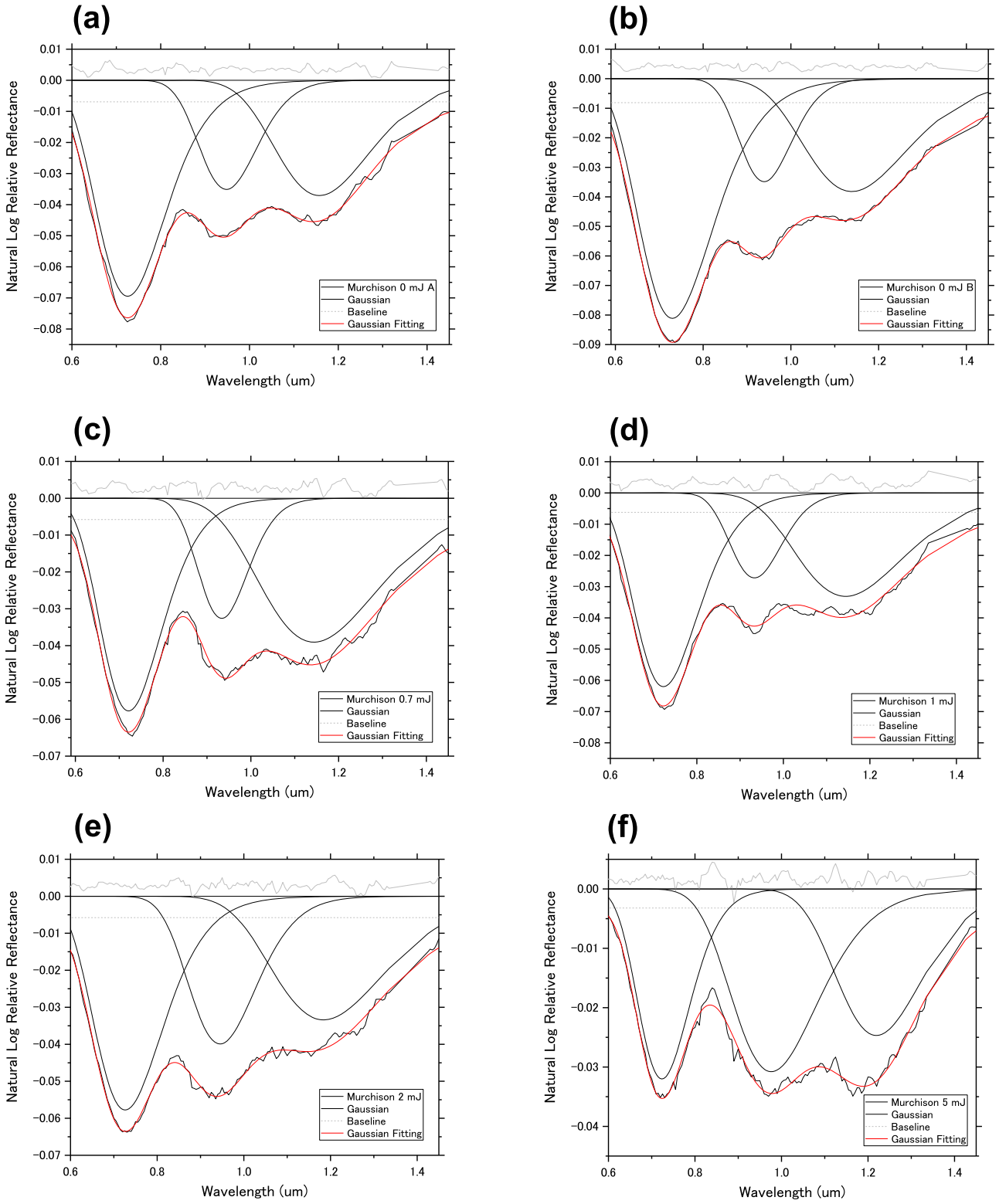

Figure 5. Modified Gaussian fitting of the 0.7, 0.9, and 1.1 μm absorption bands of untreated and laser-irradiated Murchison spectra (a)–(j). Changes in the width and center wavelength of the 0.7, 0.9, and 1.1 μm absorption bands by pulse-laser irradiation (k), (l).

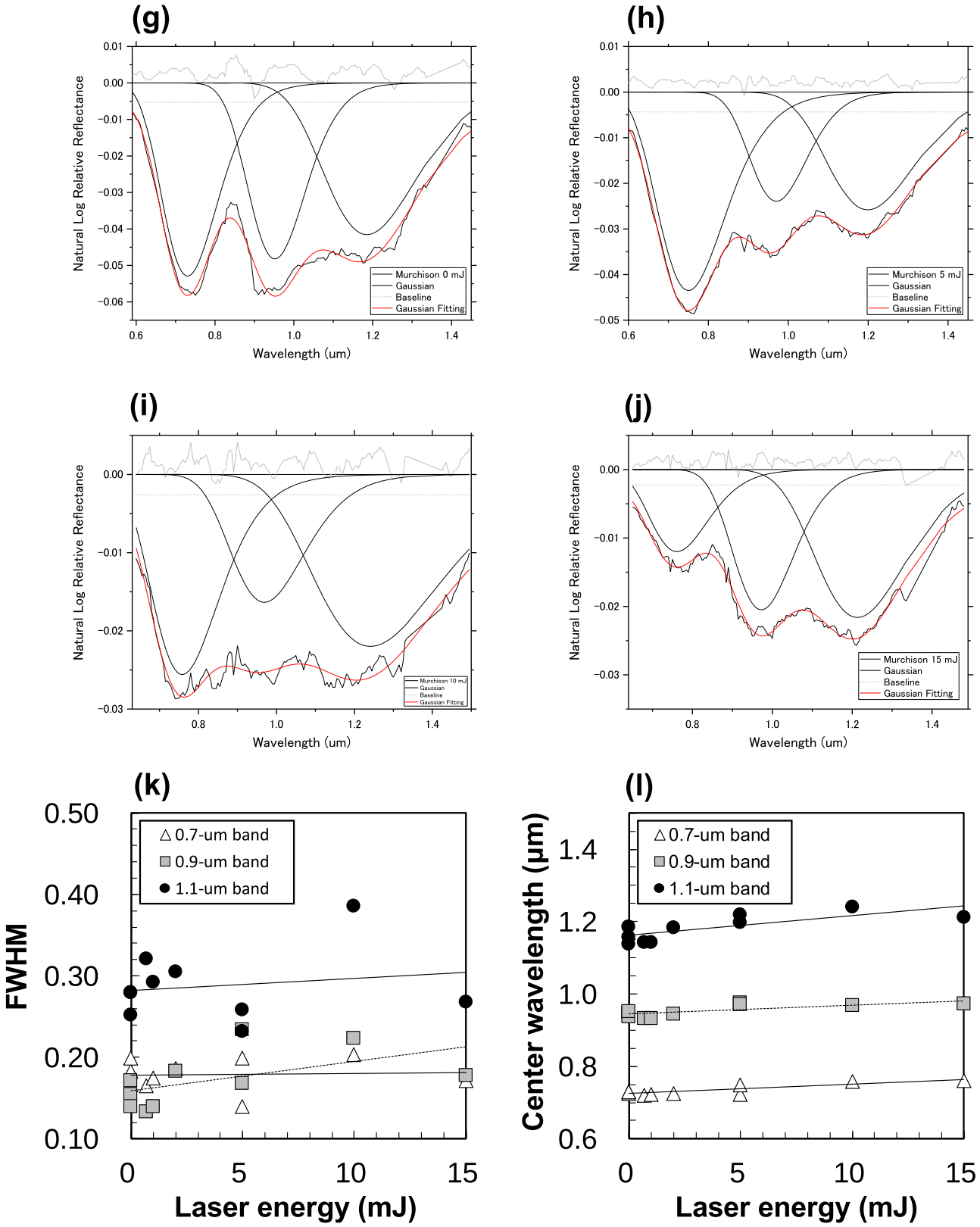

Figure 5. (Continued.)

ORCID iDs

Moe Matsuoka https://orcid.org/0000-0003-1091-3041

References

Basu, P. 2010, Biomass Gasification and Pyrolysis: Practical Design and Theory (New York: Academic)
Bennett, C. J., Pirim, C., & Orlando, T. M. 2013, ChRv, 113, 9086
Bland, P. A., Cressey, G., & Menzies, O. N. 2004, M&PS, 39, 3
Brunetto, R., Lantz, C., Ledu, D., et al. 2014, Icar, 237, 278
Brunetto, R., Pino, T., Dartois, E., et al. 2009, Icar, 200, 323
Bruno, M., Cremonese, G., & Marchi, S. 2007, PSS, 55, 1494
Busemann, H., Alexander, C. M. O. D., & Nittler, L. R. 2007, M&PS, 42, 1387
Clark, B. E., Binzel, R. P., Howell, E. S., et al. 2011, Icar, 216, 462
Clark, R. N., King, T. V. V, Klejwa, M., Swayze, G. A., & Vergo, N. 1990, JGR, 95, 12653
Cloutis, E. A., Hudon, P., Hiroi, T., Gaffey, M. J., & Mann, P. 2011, Icar, 216, 309
Cloutis, E. A., McCormack, K. A., Bell, J. F., et al. 2008, Icar, 197, 321
Duley, W. W., & Lazarev, S. 2004, ApJL, 612, L33
Gillis-Davis, J. J., Lucey, P. G., Bradley, J. P., et al. 2017, Icar, 286, 1
Hamilton, V. E., Simon, A. A., Christensen, P. R., et al. 2019, NatAs, 3, 332
Hergenrother, C. W., Maleszewski, C. K., Nolan, M. C., et al. 2019, NatCo, 10, 1291
Hiroi, T., Pieters, C. M., & Noble, S. K. 2000, LPI, 31, 1548
Hiroi, T., Sasaki, S., Misu, T., & Nakamura, T. 2013, LPI, 1719, 1276
Hiroi, T., & Zolensky, M. E. 1999, AMR, 12, 108
Hiroi, T., Zolensky, M. E., Pieters, C. M., & Lipschutz, M. E. 1996, M&PS, 31, 321
Keller, L. P., Christoffersen, R., Dukes, C. A., Baragiola, R. A., & Rahman, Z. 2015, LPI, 1878, 2010
Kelsall, T., Weiland, J. L., Franz, B. A., et al. 1998, ApJ, 508, 44
Kitazato, K., Milliken, R. E., Iwata, T., et al. 2019, Sci, 364, 272
Lantz, C., Brunetto, R., Barucci, M. A., et al. 2015, A&A, 577, A41
Lantz, C., Brunetto, R., Barucci, M. A., et al. 2017, Icar, 285, 43
Lauretta, D. S., DellaGiustina, D. N., Bennett, C. A., et al. 2019, Natur, 568, 55
Lazzarin, M., Marchi, S., Moroz, L. V., et al. 2006, ApJL, 647, L179
Mahapatra, N., Kurian, V., Wang, B., Martens, F., & Gupta, R. 2015, Fuel, 152, 29
Matsuoka, M. 2015, Master thesis (in Japanese), Tohoku Univ., Sendai
Matsuoka, M., Nakamura, T., Kimura, Y., et al. 2015, Icar, 254, 135
McAdam, M. M., sunshine, J. M., Howard, K. T., & McCoy, T. M. 2015, Icar, 245, 320
Moroz, L., Baratta, G., Strazzulla, G., et al. 2004, Icar, 170, 214
Nakamura, T., Lantz, C., Kobayashi, S., et al. 2019, LPI, 2157, 6211
Noble, S. K., Pieters, C. M., & Keller, L. P. 2007, Icar, 192, 629
Ryskin, Y. I. 1974, in The Infrared Spectra of Minerals, ed. V. C. Farmer (London: Mineralogical Society), 137
Salisbury, J. W., D'Aria, D. M., & Jarosewich, E. 1991, Icar, 92, 280
Sato, Y. 2017, Master's Thesis (in Japanese), Tohoku Univ., Sendai
Sugita, S., Honda, R., Morota, T., et al. 2019, Sci, 364, 252
Thompson, M. S., Loeffler, M. J., Morris, R. V., et al. 2019a, LPI, 2157, 6318
Thompson, M. S., Loeffler, M. J., Morris, R. V., Keller, L. P., & Christoffersen, R. 2019b, Icar, 319, 499
Vernazza, P., Fulvio, D., Brunetto, R., et al. 2013, Icar, 225, 517
Vilas, F. 2008, AJ, 135, 1101
Yamada, M., Sasaki, S., Nagahara, H., et al. 1999, EP&S, 51, 1265
Zhao, Y., Wei, F., & Yu, Y. 2010, Journal of Petroleum Science and Engineering, 74, 20